MATHEMATICAL MODELING AND COMPUTING, Vol. 12, No. 2, pp. 588–602 (2025)

Multicomponent photoionization modeling: Cloudy c23.01 vs c08.00

Melekh B. Ya., Koshmak I. O.

Ivan Franko National University of Lviv,
1 Universytetska Str., 79000, Lviv, Ukraine

(Received 1 February 2025; Revised 12 May 2025; Accepted 11 June 2025)

We present a renewed wrapper for multicomponent photoionization modeling (MPhM) of the nebular environment (NebEn) surrounding star-forming regions, based on the new version (c23.01) of G. Ferland's code CLOUDY. Our approach to MPhM of NebEn accounts for the internal structure of the HII region and its evolution driven by superwind expansion. An evolutionary grid of NebEn MPhM was calculated using both the old (based on CLOUDY c08.00) and the newly developed MPhM wrappers. The resulting ionization structures, emissivities of diagnostically important emission lines, and modeled spectra were compared to estimate the impact of a coding error related to Lyα line formation, present in the old version of CLOUDY, on the NebEn MPhM results. Based on this comparison, conclusions were drawn regarding the reliability of MPhM results obtained using the older code version.

Keywords: *nebular environment; star-forming region; photoionization modeling; superwind models.*

2010 MSC: 85-04, 85-08, 85A15, 85A25, 85A30 **DOI:** 10.23939/mmc2025.02.588

1. Introduction

Nebular objects, such as HII regions, planetary nebulae, supernova remnants, envelopes of symbiotic stars, etc., consist of highly rarefied gaseous plasmas and dust grains. To quickly determine the physical conditions and ionic abundances in nebular plasmas, so-called spectral diagnostic methods are commonly used [1]. These methods do not account for the radiative transfer of ionizing photons and rely on diagnostic ratios between emission lines.

In spectral diagnostic methods, the nebular environment (NebEn) is typically divided into ionization zones, each assumed to have uniform physical conditions and ionic abundances throughout its volume. This assumption is significantly inaccurate for inhomogeneous NebEns. A more accurate approach involves photoionization modeling of nebular objects [1], which is based on solving the radiative transfer equation through the nebular plasma and accounting for important elementary processes induced by this transfer.

In such modeling, the nebular object is divided into numerous small volumes, each of which is sufficiently small to achieve the desired computational precision. Within each of these volumes, the solution of the ionization-recombination equilibrium equations provides ionic abundances. The statistical equilibrium equations determine the populations of energy levels of the relevant atoms and ions, while the energy balance equation iteratively determines the electron temperature (for further details, see [1, 2]).

As highlighted in [3–6], accounting for the internal structure and evolution of giant HII regions surrounding star-forming knots is critically important for accurate photoionization modeling. The evolution of these NebEns is significantly influenced by the presence of superwinds originating from the central star-forming area.

This work is done in the framework of the project *"Tomography of the Dark Ages and Cosmic Dawn in the lines of hydrogen and the first molecules as a test of cosmological models"* (state registration number 0124U004029) supported by National Research Found of Ukraine.

Two approaches were proposed in [5, 6] to address this:

1. Utilizing self-similar (automodeling) solutions [7, 8] of the hydrodynamical equations governing the evolution of stellar wind and superwind bubbles.
2. Basing photoionization modeling on the results of chemodynamical simulations of dwarf galaxies undergoing active star formation.

In [5, 6], we proposed methods for multicomponent photoionization modeling (MPhM) of NebEns in dwarf galaxies with active star formation. The first approach is planned to be applied in the task of modeling the spectral energy distribution (SED) of the earliest dwarf galaxies, embedded in halos containing a mixture of ordinary and dark matter and hosting either the first stars or Population II ones.

As concluded in [9], it is highly probable that the first dwarf galaxies were the primary sources of the Universe reionization. To derive the corresponding SEDs, it is essential to account for the transfer of ionizing radiation from the central stars through the surrounding NebEn. The proposed NebEn MPhM approach enables such detailed modeling.

The MPhM approach is based on the photoionization code developed by G. Ferland [2]. In [3–5], we used the NebEn MPhM wrapper based on CLOUDY c08.00. In [10], the updated CLOUDY c23.01 was announced, along with a critical notification that a simple coding error, present since ≈1990, had been corrected. This error occurred in a routine requiring conversion from line-center to mean normalization of the Lyα optical depth [10].

According to [10], this correction affects the destruction of H I Lyα by background opacities, with the largest impact observed in high-ionization dusty clouds, where the predicted Lyα intensity can be up to three times stronger. During NebEn MPhM of HII regions in star-forming dwarf galaxies, the density of matter varies over a wide range – from 0.05 to 100 cm^{-3}. Additionally, the models presented in [3–5] include dust with various abundance values.

Therefore, it becomes essential to verify the reliability of past NebEn MPhM results and to ensure that future calculations, particularly for the first dwarf galaxies, are accurate and unaffected by this coding issue.

To address this task, we have developed a new wrapper for MPhM based on the updated version of the CLOUDY code, c23.01. The aim of this paper is to perform a comparative analysis of typical MPhM calculation results, obtained using both the old and new versions of CLOUDY – c08.00 and c23.01, respectively.

In Section 2, we briefly describe the algorithm for MPhM of HII regions in star-forming galaxies. Section 3 presents a comparison of the resulting ionization structures, emissivities in diagnostically important spectral lines, and corresponding emission line spectra, as well as the transformation of the SED during the passage of ionizing radiation through model components, as calculated using the new and old versions of CLOUDY.

Finally, in the Conclusions, we discuss the reliability of the old MPhM version and summarize the obtained results.

2. Multicomponent photoionization modeling of HII regions in dwarf star-forming galaxies

A detailed description of our technique for MPhM of NebEn in star-forming galaxies and its evolution can be found in [11–13]. Specifically, in [11], the gas density was assumed to vary between different components of the bubble but remained constant within the volume of each component. More complex multicomponent models were developed in [12], where the theory of bubble-structure evolution proposed by Weaver & Castor [8] was employed to describe the density and temperature distributions within the superwind region (SWR).

Here, we present the latest algorithm for MPhM, detailed in [5], which differs from previous approaches by incorporating the Chevalier and Clegg [7] model to define the temperature distribution in

the superwind free expansion region (the first component in our simulations). The simulation terminates when the pressure at the external boundary of the bubble equals that at the inner edge of the surrounding HII region, as this condition signifies the cessation of the superwind bubble's expansion. At this stage, it is highly likely that the adopted SWR structure begins to decay due to hydrodynamic instabilities.

As described in [13], the central star-forming region is the main source of ionizing radiation during MPhM of HII regions. The superwind blowing out from this region forms a shock wave that compresses the surrounding nebular gas and creates a thin, dense shell [8]. The reverse shock wave thermalizes the rarefied gas in the cavity [8]. As a result, the superwind cavity emits thermal radiation at very high temperatures (sometimes exceeding 10^6 K).

The complex structure of the surrounding NebEn is divided into four main components (see Figure 1):

1. The first component represents the superwind, freely expanding from the central star-forming region.
2. The second component represents the hot, rarefied gas in the superwind cavity, heated by the reverse superwind shock.
3. The third component represents the high-density shell compressed by the direct superwind shock-wave.
4. The fourth component represents the hydrodynamically undisturbed, photoionized HII region.

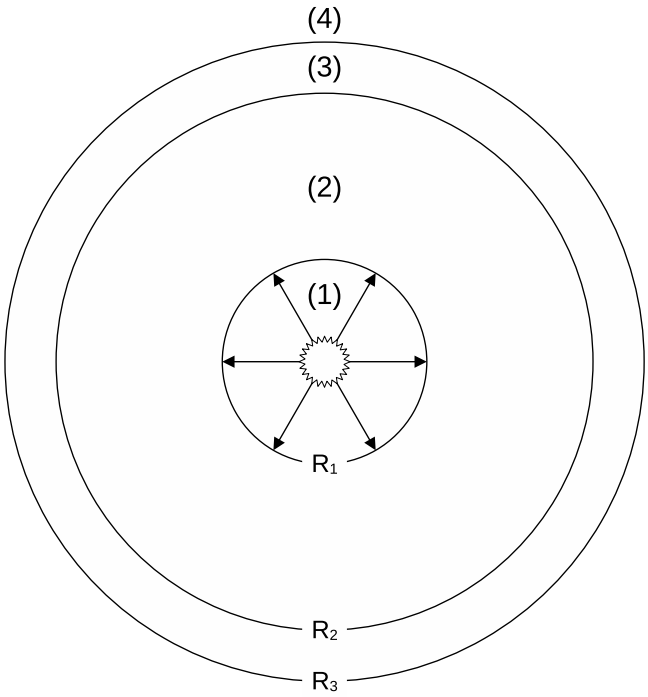

Fig. 1. Structure of the multicomponent photoionization model of HII region.

Each modeling component represents a separate spherically symmetric photoionization model. The photoionization in each of these components is caused by two types of radiation quanta:

— Quanta of direct radiation from the ionization source (stars), which are not absorbed in the previous component;
— Quanta of diffuse ionizing radiation emitted in the previous and present components (calculated using the outward-only approximation [14]).

The internally incoming Lyman continuum (Lyc) spectra radiated by stars located within the central star-forming region were calculated using the evolutionary synthesis code STARBURST 99 [15], assuming continuous star formation with a star formation rate (SFR) of 0.0267 $M_\odot \cdot \text{year}^{-1}$. The initial

mass function (IMF) slopes correspond to the Kroupa distribution: -1.3 for stellar masses in the range of 0.1 to 0.5 $M_\odot$, and -2.3 for stellar masses between 0.5 and 100 $M_\odot$.

Evolutionary tracks from the Geneva v40 models (with a starting rotation rate of 40% of the parabolic velocity at zero age on the main sequence) for a metalicity of 0.001 were used. The Maeder wind model [16,17] was adopted. We begin the simulation at an age of 10 kyr and continue until 20 Myr, with a timestep of 10 kyr. The grid is based on Pauldrach/Hillier stellar atmosphere models [18]. The microturbulence velocity in the atmospheres of red giants, which was used to calculate the near-infrared spectrum, is set to 3 km/s.

The chemical abundances of elements escaping into component 1 due to the superwind and supernova explosions in component 1, as well as the rate of mass loss by the star-forming region to the superwind, $\dot{M}_\mathrm{w}$, at the aforementioned value of SFR, and the mechanical luminosity L_w were also obtained using the evolutionary-population synthesis code STARBURST 99 [15]. All these parameters were used as input for MPhM of the HII region.

The chemical abundances inside component 2 were determined by averaging over the mass of components 1 and 3, due to matter evaporation at the boundary between components 2 and 3 (see below and [8]).

The metalicity of the outer components (3 and 4) was adopted according to the oxygen abundance of $12+\lg(\mathrm{O/H}) = 7.117$. Gas abundances of Ne/H, S/H, Ar/H, and Fe/H in the 3rd and 4th components of the H II region were determined using approximation expressions that define their dependence on the abundance of O/H (see [4]). These expressions were obtained from the results of [19, 20].

To determine the abundances of C/H, Mg/H, Si/H, and Cl/H in the 3rd and 4th components, we adopted the gas abundances within the HII region, as established at the Meudon and Lexington meetings [2, 21, 22], for the calculation of photoionization models of the standard HII region. For each model, the abundances of C/H, Mg/H, Si/H, and Cl/H were obtained as the product of the corresponding adopted basis composition and the fixed *gas metalicity factor*, determined as the ratio of oxygen abundances at the current metalicity to the one adopted as the basis abundance, respectively.

In the 3rd and 4th components, the presence of dust grains was also taken into account during the MPhM. The dust particle distribution over their sizes was taken from [2,23]. Similarly to [4,24], the dust is represented as a mixture of silicate and carbonate grains, with the basis abundance corresponding to the interstellar medium modeling. In the models, this dust abundance was renormalized by the *dust metalicity factor*, determined in a similar way to the *gas metalicity factor* described above.

The temperature distribution for the first component was calculated according to the Chevalier and Clegg model [7]:

$$T_1 = 0.0106 \cdot \left(\frac{r}{r_0}\right)^{-\frac{10}{3}} \cdot \dot{M}_\mathrm{w}^{\frac{1}{2}} \cdot {L_\mathrm{w}}^{\frac{1}{2}} \cdot {r_0}^{-2}\ [K], \quad (r_0 = 1\,\mathrm{pc}). \tag{1}$$

Taking into account the data from [8], the velocity in the first component corresponds to the stellar superwind velocity, $v_1 v_\mathrm{w}$ [km/s].

The number density in the first component was calculated in accordance with the data from [7,25]:

$$n_1 = \frac{\dot{M}_\mathrm{w}}{4 \cdot \pi \cdot r^2 \cdot ChF_{in} \cdot m_\mathrm{H} \cdot v_\mathrm{w}} \quad \left[\mathrm{cm}^{-3}\right]. \tag{2}$$

Here, r represents the distance from the starburst, m_H is the mass of a hydrogen atom, and ChF_{in} is the total abundance of all chemical elements relative to hydrogen for the internal components [4].

The second component is located between the inner radius, R_1, and outer radius, R_2, which were determined using expressions from [8] at the required ages. The mass of the first component, M_1, can then be calculated.

The physical conditions along the radius of the second component are obtained as the solution of the continuity and energy transfer equations, accounting for thermal conductivity [8]. The boundary conditions under which this system was numerically solved, along with the solution itself (the distribution of the dimensionless electron temperature, τ, and the expansion rate, u, over the dimensionless

radial coordinate, ξ), are described in detail in our previous studies [4, 24]. By multiplying the values of τ and u by the relevant factors provided in [8], we derive expressions for the distributions of the electron temperature (T_2), expansion rate (v_2), and density (n_2) in the second component [13]:

$$T_2 = TF \cdot \tau \ [K],$$

$$TF = 9.65 \cdot 10^5 \cdot n_0^{\frac{2}{35}} \cdot \left(\dot{M}_6 \cdot v_{2000}^2\right)^{\frac{8}{35}} \cdot t_6^{-\frac{6}{35}}; \tag{3}$$

$$\dot{M}_6 = \frac{\dot{M}_{\rm w}}{10^{-6}\ M_\odot/yr},$$

$$v_{2000} = \frac{v_w}{2000\ \text{km/s}}, \quad t_6 = \frac{t}{10^6\ \text{yr}},$$

$$v_2 = VF \cdot u \ [\text{cm/s}], \quad VF = \frac{3}{5} \cdot \frac{R_2}{t}. \tag{4}$$

If the process is isobaric, then

$$n_2 = DF \cdot (1/\tau) \ [\text{cm}^{-3}], \tag{5}$$

$$DF = \frac{M_2}{\frac{4}{3} \cdot \pi \cdot ChF_{mix} \cdot m_{\rm H} \cdot ({R_2}^3 - {R_1}^3)}.$$

Here, ChF_{mix} represents the total abundance of all chemical elements relative to hydrogen in the second component. The abundance of each chemical element in this component was determined as a mixture of the chemical abundances within the first and third components, averaged over mass, using the following expression: $\left(\frac{A}{H}\right)_{mix} = \left(\frac{A}{H}\right)_1 \cdot \left(1 + \frac{H_3}{H_1}\right)^{-1} + \left(\frac{A}{H}\right)_3 \cdot \left(1 + \frac{H_1}{H_3}\right)^{-1}$, where indices 1 and 3 refer to the abundances of chemical elements in the first and third components, respectively.

The mass of the second component, M_2, was determined as follows:

$$M_2 = (M_{sb} - M_1) + \int_0^{age} \dot{M}_b dt,$$

where $\dot{M}_b$ represents the rate of gas mass evaporation from the third component into the second component (see details below).

For each model, these dependencies must be rescaled according to the values of R_1 and R_2.

The electron temperature in the third and fourth components was determined during the photoionization modeling by solving the energy balance equation.

As described in [13], the gas density n_3 in the dense thin layer (third component) was calculated based on the isobaric conditions at the contact discontinuity between the second and third components. The outer radius of the third component was established during the photoionization modeling process, using the known mass of the third component, which is determined as follows:

$$M_3 = \frac{4}{3} \cdot \pi \cdot ChF_{out} \cdot m_{\rm H} \cdot n_0 \cdot r_2^3 - \int_0^{age} \dot{M}_b \, dt.$$

This is the mass of gas compressed by the outer (direct) shock. Here, ChF_{out} represents the total abundance of all chemical elements relative to hydrogen, specifically for the external components. The mass M_3, reduced by the amount of gas evaporated from the third component into the second one [25], can be expressed as follows:

$$\dot{M}_b = \frac{16}{25} \cdot \frac{\mu}{k} \cdot C \cdot {T_b}^{5/2} \cdot R_2,$$

where

$$T_b = 1.6 \cdot 10^6 \cdot {n_0}^{2/35} \cdot \left(\dot{M}_6 \cdot v_{2000}\right)^{8/35} \cdot {t_6}^{-6/35} \ [K] \tag{6}$$

is the central temperature within 2nd component.

As described in [13], the MPhM was terminated upon achieving pressure balance at the boundary between the third and fourth components. The outer radius of the third component and the corresponding age at which this equilibrium occurs are referred to as the stagnation radius and stagnation age, respectively. Under these conditions, the expansion of the bubble halts, and it is likely that the third component undergoes fragmentation, followed by the decay of the adopted SWR structure due

to hydrodynamic instabilities. These processes are not included in our simulations; thus, calculations for each evolutionary sequence of models are concluded at the stagnation age.

This approach enables us to track the evolution of key physical parameters of such a complex multicomponent NebEn and analyze the emission line spectra originating within it.

3. Models calculation and comparison

We calculated an evolutionary grid of four-component MPhMs, as described in detail in the previous section, using two versions of the CLOUDY code: c08.00 [2] and c23.01 [10]. In this section, we compare the MPhM results for two specific evolutionary stages: 1 Myr and 7 Myr. The first age represents the early stage of star-forming region evolution, while the second age is of interest due to the significant impact of the first supernovae on the NebEn.

The ionization structure of the NebEn is influenced by the ionizing radiation (Lyc spectra), as well as by the spatial distributions of electron temperature, T_e, and electron density, n_e, which govern the distribution of ion abundances. These parameters, in turn, determine the emissivities of key emission lines, which are used to compute model fluxes within synthetic apertures. Comparing these fluxes with observed ones serves as the primary method for assessing the reliability of MPhMs. Below, we analyze and compare the parameters obtained using the c08.00 and c23.01 versions of CLOUDY.

3.1. Lyc-spectrum transformations

The ionization structure of the NebEn is defined by its density and chemical abundances, as well as by the transfer of ionizing radiation through the environment, and in some cases, by shocks. Superwind shocks result in complex density and temperature distributions within components 1 and 2, while the emission lines critical for nebular diagnostics predominantly form in components 3 and 4, where shocks are absent. However, the density in component 3 is influenced by hydrodynamical processes occurring in components 1 and 2.

The transfer of ionizing radiation through the first two inner components can significantly alter the shape of the Lyc spectra emitted by the star-forming region. The ionization structure in components 3 and 4 is governed by the Lyc spectrum emerging from the preceding internal nebular components. Therefore, comparing the Lyc spectra exiting components 2 and 3 is crucial (see Figure 2).

A comparison of the output spectra from components 2 and 3, shown in Figure 2, reveals that the differences are primarily driven by the absorption of ionizing photons in component 3, predominantly through photoionization processes. This absorption increases with age due to the expansion of the components (including component 3), which leads to an increase in the optical thickness of component 2. The most pronounced differences, caused by photoionization, are observed at photon energies exceeding 4 Ryd.

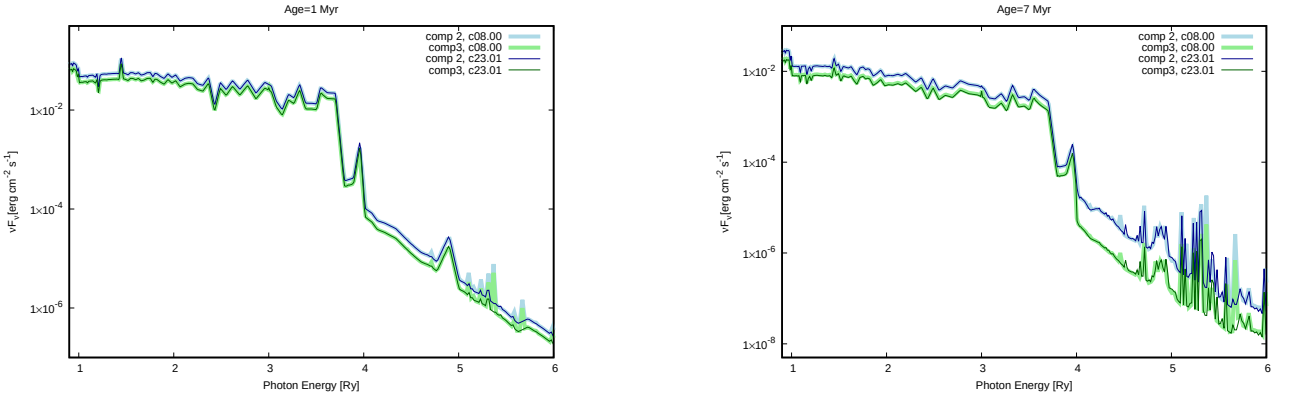

Fig. 2. Comparison of Lyc-spectra outgoing from 2nd and 3rd components 2 obtained during calculations of MPhMs for 1 Myr and 7 Myr using c08.00 and c23.01 releases of code CLOUDY, correspondingly.

The main difference between the results of c08.00 and c23.01 is observed at photon energies exceeding 4 Ry, where high-energy ionizing emission lines are present. It is evident that the intensities of

these lines are lower in the results obtained with the newer version of CLOUDY for both components. Notably, the relative differences are more significant at 1 Myr. Interestingly, c08.00 predicts the presence of two "phantom" emission lines in the photon energy range between 5 Ryd and 6 Ry, which are absent in the spectrum calculated using c23.01.

The new version of CLOUDY employs a much finer photon energy resolution grid and resolves several bugs present in earlier versions, including the issue highlighted in the Introduction. Consequently, the spectrum produced by c23.01 is considered more accurate than that of c08.00. However, it is essential to note that component 2 is dust-free. As mentioned earlier, the most significant impact of the error in c08.00, related to the calculation of Lyα intensity, is expected in high-ionization *dusty* clouds.

The differences described above are consistent for the outward spectra from both component 2 (dust-free) and component 3 (dusty). Thus, these discrepancies are unlikely to result from the code error in c08.00 discussed in the Introduction. Nonetheless, the primary differences occur in the photon energy range where the radiation flux is $4-5$ orders of magnitude lower than at photon energies $\leqslant 4$ Ryd. Therefore, it can be concluded that these differences do not have a significant impact on the ionization structures of components 3 and 4.

3.2. Electron temperatures

The radial electron temperature, T_e, distributions within the first two components are defined by Expressions (1) and (4), and therefore, their distributions are identical in both versions of the CLOUDY code.

In Figure 3, the temperature distributions with depth within components 3 and 4 are shown. As demonstrated in our previous works (see e.g. [5]), these components are responsible for the emission of most of the observed spectral lines.

The differences between values of T_e for component 3 (left figure) obtained using c08.00 and c23.01 are less than 0.62% at the inner edge of this component for 1 Myr, and less than 0.24% for 7 Myr at a depth of 100 pc. It can be seen that after expansion, the difference in the thickness of the 3rd component is larger for the age of 7 Myr: $> 13\%$ vs $\approx 1\%$ for 1 Myr.

In the case of component 4 (right figure), these differences reach 5.93% at 3 kpc for 1Myr and approach 1% at 4.5 kpc for 7 Myr. It should be noted that the thickness of both components 3 and 4 calculated using c23.01 is larger than that calculated using c08.00. However, these small differences cannot cause significant variations in the resulting emission line spectrum of the models (see below).

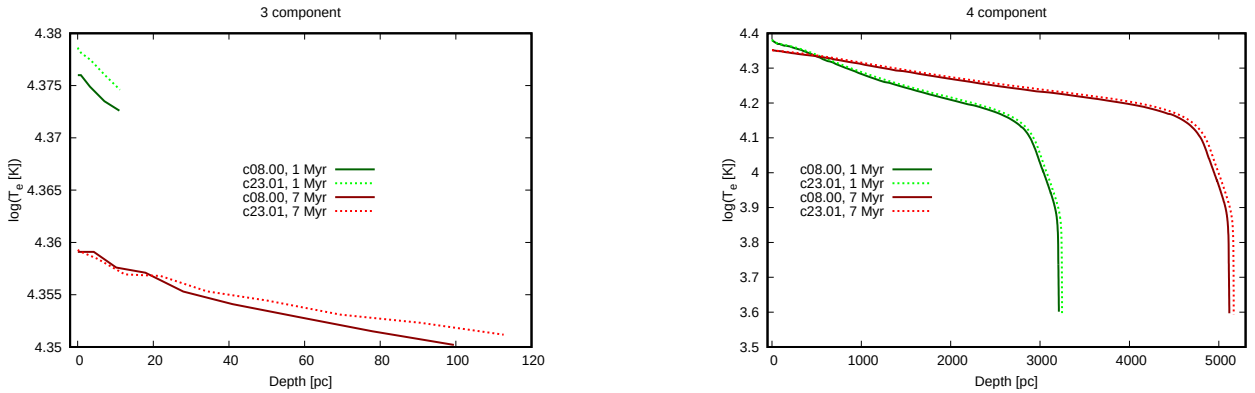

Fig. 3. Comparison of electron temperature distributions within components 3 and 4 of the NebEns obtained from MPhMs based on c08.00 and c23.01 releases of the CLOUDY code. In this and all subsequent figures, the depth parameter, instead of Radius, is used. Depth is equal to zero at the inner radius of the corresponding component.

3.3. Electron densities

As mentioned earlier, while the density in component 4 is related to input parameters (we adopted it to be 0.05 cm^{-3}), the radial density distributions in the first two components are defined by Expressions (2)

and (5), and in component 3, it is determined using isobaric conditions at the contact discontinuity between the 2nd and 3rd components. The electron density, n_e, is mainly defined by the gas density and its chemical abundances, but it also depends on radiative transfer (due to photoionization) and electron temperature (due to collisional ionization). Therefore, n_e is determined during MPhM using the requirement of plasma electroneutrality.

The comparison of the radial n_e dependence obtained using c08.00 and c23.01 versions of the CLOUDY code is shown in Figure 4. In the first two components, n_e is primarily defined by the corresponding radial density distributions. In the 1st component, n_e values obtained using c23.01 are higher (up to 25.3% at the outer edge for 1 Myr and more than 136% for 7 Myr) compared to those obtained from c08.00. In the 2nd component, the opposite result is observed (up to 9.3% for 1 Myr at a depth of 36 pc and $> 24\%$ for 7 Myr at a depth of 200 pc). It should be noted that in the 1st component, such large differences are found at very low densities, which reduces their impact on the differences in modeling the emission line spectra.

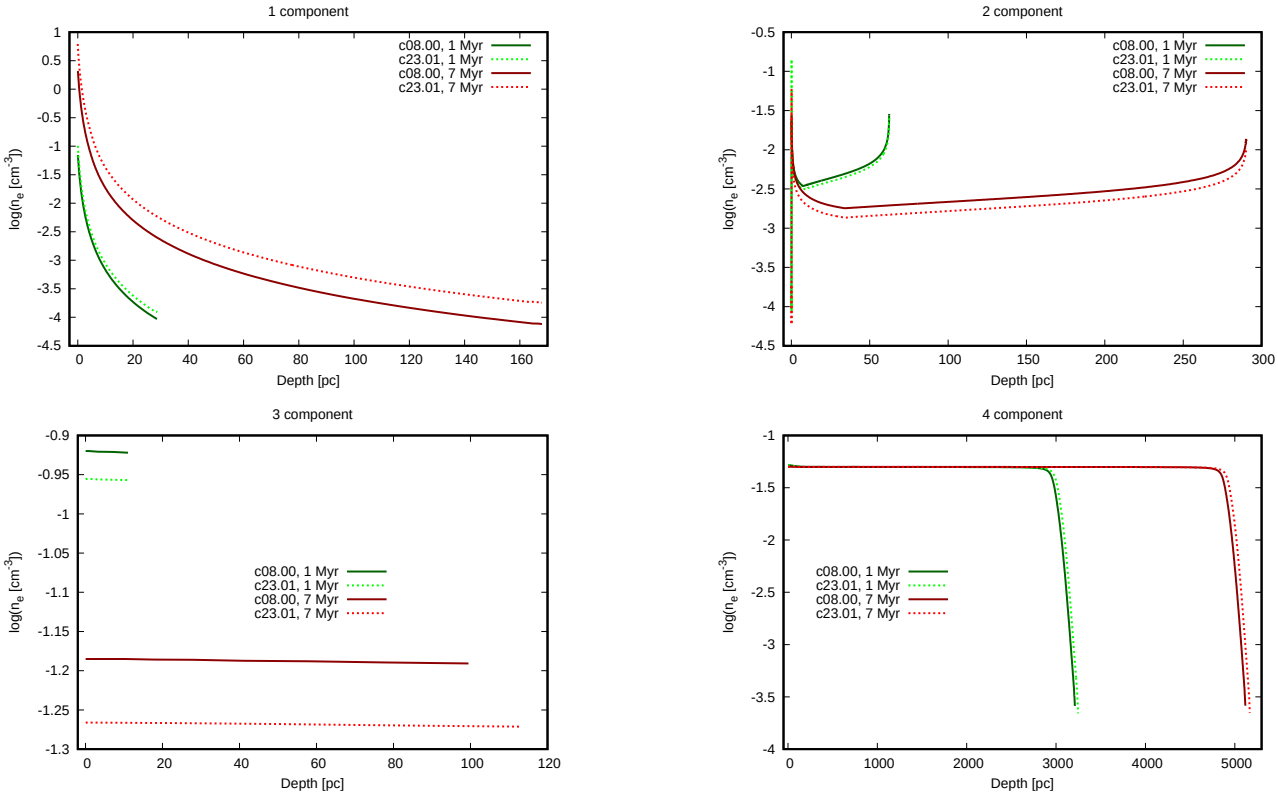

Fig. 4. Comparison of the electron density distributions within the corresponding components of the NebEns obtained from MPhMs based on c08.00 and c23.01 releases of the CLOUDY code.

In the 2nd component, the n_e values in the 3rd component, obtained using c08.00, are higher than those from c23.01. The differences between these results are due to the differences in densities obtained from isobaric conditions at the contact discontinuity between the 2nd and 3rd components. The density resolution of c23.01 models (defined by the number of modeling shells) is much higher than that of the c08.00 models, making the c23.01 results more accurate. The difference increases with age: 8% for 1 Myr models and 17% for 7 Myr models.

In the 4th component, the differences between the old and new CLOUDY results are due to the slightly larger volume of ionized gas in the c23.01 case.

3.4. Emissivities and emission line spectrum

The ionization structure of the nebular gas defines the spectral line emissivities, which allow the calculation of the entire modeled emission line spectrum or, in cases of complicated geometry, in synthetic apertures (see, for example, [6, 26]).

It should be noted that while the emissivities of recombination lines depend on the abundance of the chemical element in an ionization stage one unit higher than the ionization stage of the emitting ion, the emissivity of forbidden emission lines depends on the abundance of the emitting ion. This is because the primary reason for populating metastable energy levels is collisional excitation by free electrons.

The emissivity of the recombination line HeIIλ4686 (see Figure 5) shows a dependence on depth in the first two components similar to the electron density distribution (see Figure 4). It exhibits a maximum where both the temperature and density reach their highest values. While the maximum temperature value leads to the highest He^{++}/He fraction, the highest density value at these conditions results in the maximal He^{++} abundance.

From Figure 5, it can be seen that for an age of 1 Myr, the HeIIλ4686 emissivity reaches its maximum at the inner edge of the 2nd and 3rd components. However, in the 2nd component, this emissivity decreases rapidly with depth. As a result, the largest contribution to the total luminosity of the NebEn in the HeIIλ4686 emission line at this age comes from the 3rd component, as well as the inner part of the 4th component, where the emissivity decreases more slowly than in the 2nd component.

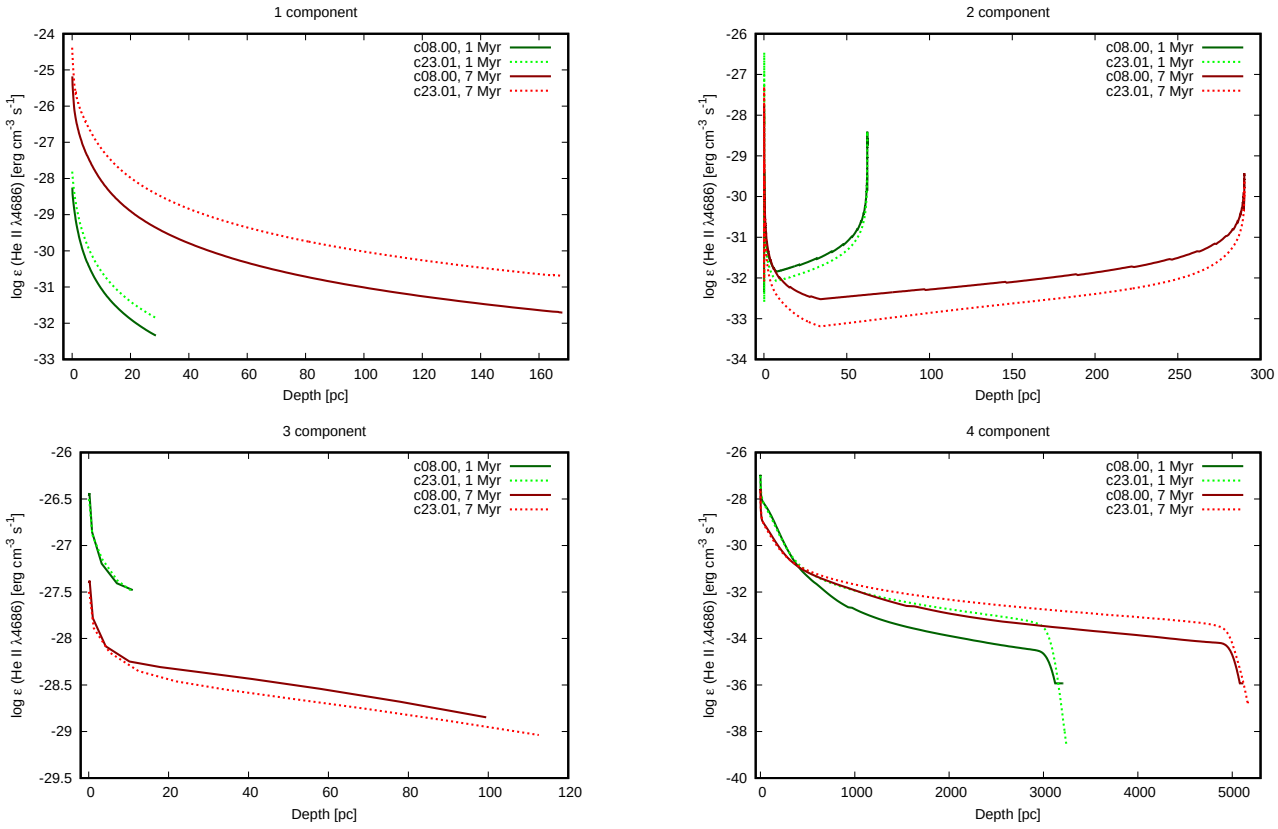

Fig. 5. Emissivity of the recombination line He IIλ4686 obtained from MPhMs based on c08.00 and c23.01 releases of the CLOUDY code, respectively.

On the other hand, for an age of 7 Myr, the HeIIλ4686 emissivity reaches its maximum at the inner edge of the 1st component. This difference is related to the increasing density in the 1st component at ages of $4-7$ Myr, due to supernova explosions.

In Figure 5, it is clear that the difference between the emissivity behaviors obtained using the c23.01 and c08.00 codes increases as the value of this quantity decreases. Therefore, in the 1st component, at this age, the drop in emissivity is much slower for the c23.01 results, leading to different conclusions regarding the contribution of various components to the total HeIIλ4686 luminosity. In the case of c23.01, it is the 1st component that contributes most, while in the case of c08.00 results, it is the 3rd component. This is a serious conclusion regarding the safety of using older versions of CLOUDY (prior

to c23.01) to analyze the emissivities of highly ionized ions in NebEns characterized by low densities and high temperatures.

Additionally, it is clearly seen that the lower limit of 10^{-36} manifests itself in the transition of the emissivity dependence into a horizontal line parallel to the depth axis when this value is reached (close to the outer edge of the 4th component).

In the case of the Hα recombination line (see Figure 6), its behavior within the 1st and 2nd components is similar to that of HeIIλ4686. The difference arises in the 3rd and 4th components. The ionization potential of H^0 (1 Ryd) is lower than that of He^+, therefore the H^+/H fraction is close (but not equal!) to unity over the entire nebular volume of components $1-3$ and over most of the volume within the 4th component. Only near the ionization front (the outer edge of component 4) does H^+ transition to the H^0 stage, and the shell where this transition occurs is very thin compared to the total thickness of this component.

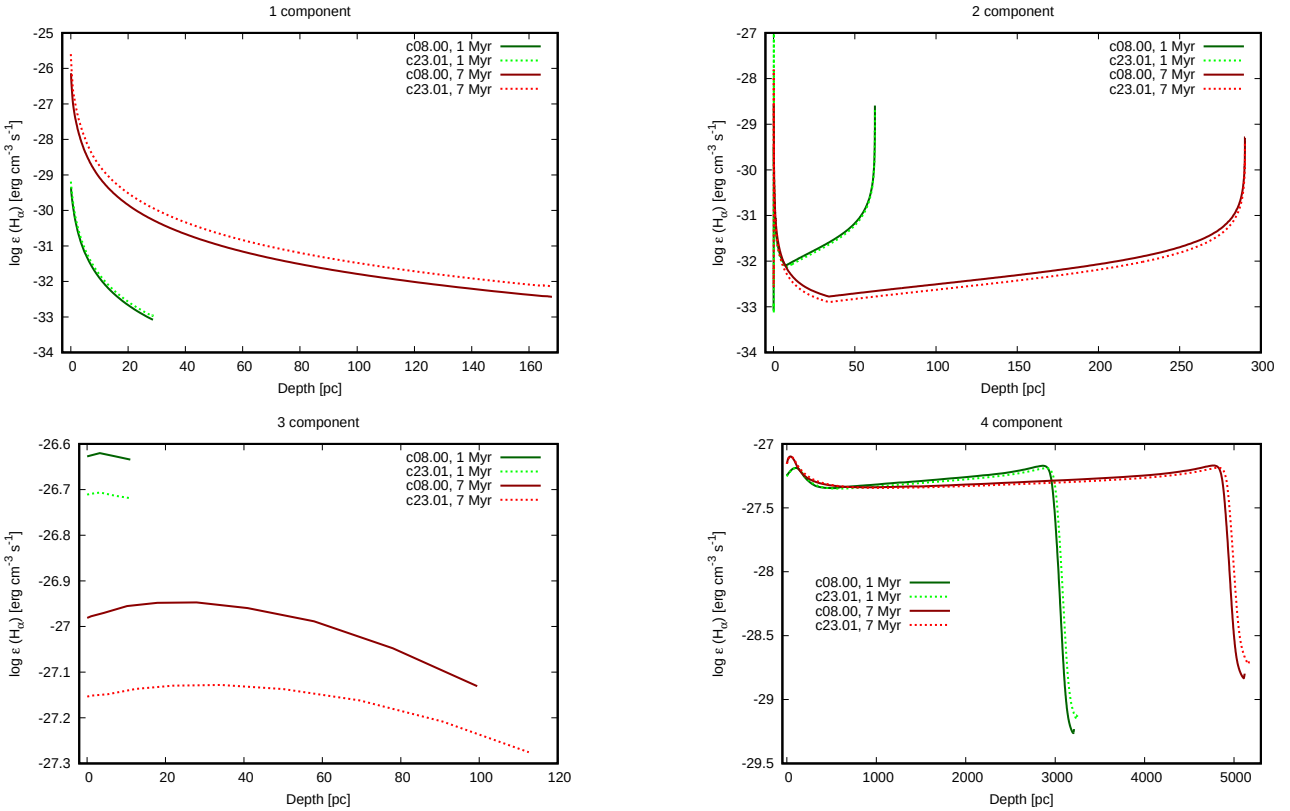

Fig. 6. The emissivity of the recombination line H_α, obtained from MPhMs based on the c08.00 and c23.01 releases of the CLOUDY code, respectively.

The first emissivity maxima in the 3rd and 4th components are caused by the increase in the total ionizing radiation flux with depth up to the maximum location. This occurs due to the rise in the total diffuse ionizing flux, which increases with depth faster than the decrease of direct ionizing radiation from the previous component (which includes direct ionizing radiation attenuated by absorption in previous components and diffuse ionizing radiation emitted there). The attenuation of diffuse ionizing radiation due to its absorption from the emitting point to the modeling point was also taken into account. At depths beyond the maximum location, absorption dominates and the emissivity decreases with depth.

However, component 4 is much more extended than the 3rd component. Therefore, the decrease in the total ionizing flux with depth causes a drop in the electron temperature (see Figure 3 for the 4th component). This decrease in T_e results in a reduction in the hydrogen recombination rate, which in turn leads to an increase in the emissivities of hydrogen recombination emission lines, particularly the Hα emissivity. Additionally, the decrease in the total abundance of ions of other chemical elements,

which could trap free electrons, occurs while the H^+/H fraction remains close to unity. As a result, the fraction of electrons available for recombination with H^+ ions increases with depth, until a depth is reached near the ionization front where the H^+/H fraction starts to drop rapidly. These factors together lead to the presence of a second maximum of the Hα emissivity in the 4th component.

The largest deviation of the c23.01 Hα emissivity from the c08.00 results in the 1st component occurs near its outer edge. However, this deviation is much smaller than the one observed for the HeIIλ4686 emissivity. It should also be noted that under the physical conditions in this component, the c08.00 Hα emissivity decreases faster than the c23.01 emissivity. As in the case of the HeIIλ4686 emissivity, the Hα emissivity shows a maximal deviation at the position of the minimum, but the deviation is much smaller than for HeIIλ4686.

Unlike the HeIIλ4686 emissivity, the Hα emissivity in the 3rd component shows the largest deviation between the c23.01 and c08.00 results close to the maximum location of this quantity. The differences in the results are caused by slightly different density determinations through the isobaric condition, as c23.01 has much higher spatial resolution than c08.00.

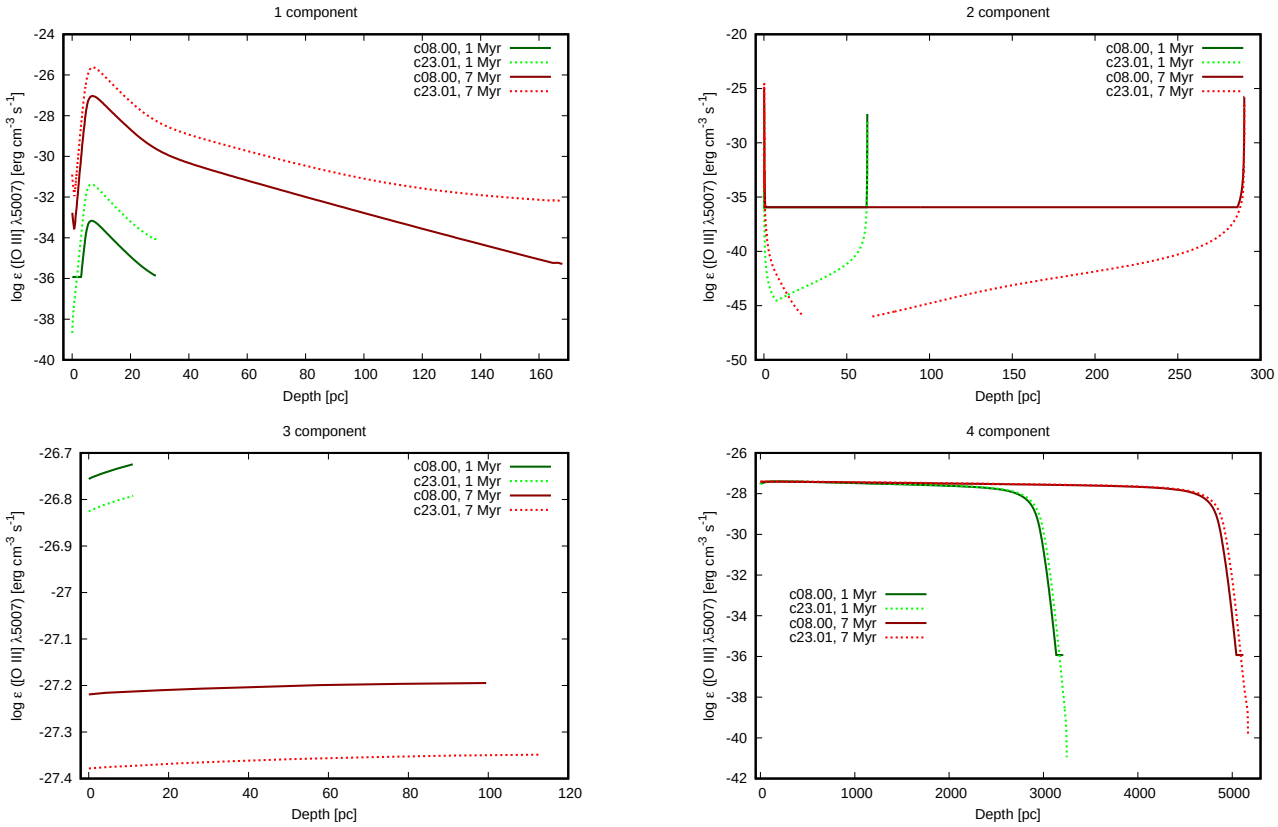

Fig. 7. The emissivity of the brightest forbidden emission line in the optical range, [OIII]λ5007, obtained from MPhMs based on the c08.00 and c23.01 releases of the CLOUDY code, respectively.

The differences in the results for component 4 are very small (less than 5%) compared to those for the HeIIλ4686 emissivity. However, it should be noted that in component 4, the c08.00 Hα emissivity reaches slightly larger values than the c23.01 one. Therefore, the contribution of this component to the total luminosity in Hα may be slightly less in the case of the c23.01 results.

The emissivity values of forbidden lines are mainly determined by the populations of metastable levels (transitions from which to lower ones lead to the appearance of photons in these lines) through collisional impacts with free electrons. That is why these lines are frequently referred to as collisionally excited lines. Of course, there is also a contribution to these populations from recombination processes, but under physical conditions in nebular plasmas, the collisional excitation mechanism remains dominant.

The population of the corresponding metastable level depends on the local electron density and temperature. Additionally, the emissivity values of forbidden lines depend on the abundance of the emitting ion. As an example, in Figure 7, we compare the emissivity depth dependence of the brightest forbidden emission line in the optical range, [OIII] λ5007, obtained using the c08.00 and c23.01 codes. It can be seen that the character of the dependence from both codes is similar within the 1st component (both show a similar location for the maximum), but the emissivity values are quite different: more than an order of magnitude difference in the inner part of the 1st component and $2-3$ orders of magnitude difference in the outer part. This fact increases the impact of the 1st component in the formation of the [OIII] λ5007 emission line flux.

Table 1. Comparison of emission line spectra obtained for 1 Myr and 7 Myr using c08.00 and c23.01 releases of the CLOUDY code.

Relative intensity	c08.00 (1 Myr)	c23.01 (1 Myr)	c08.00 (7 Myr)	c23.01 (7 Myr)
[O III]λ5007/Hβ	0.906	0.929	1.095	1.123
[O III]λ4959/Hβ	0.301	0.311	0.364	0.376
[O III]λ4363/Hβ	0.022	0.023	0.028	0.029
[O II]λ3727/Hβ*	0.404	0.393	0.340	0.331
[O III]λ5007/[O II]λ3727	2.244	2.365	3.223	3.390
[S II]λ6716/Hβ	0.022	0.022	0.016	0.017
[S II]λ6731/Hβ	0.016	0.016	0.012	0.012
H α/Hβ	2.927	2.829	2.901	2.808
[N II]λ6584/Hα	0.0047	0.0049	0.0036	0.0037
[S II]λ6716/Hα	0.0075	0.0079	0.0056	0.0059
[S II]λ6731/Hα	0.0053	0.0055	0.0040	0.0041
[S II] (λ6716+λ6731)/Hα	0.013	0.013	0.0096	0.0100

*[O II]λ3727/Hβ = [O II] (λ3726+λ3729)/Hβ.

Nevertheless, it can be seen from Figure 7 that the 4th component is the most extended. Therefore, despite the fact that the emissivity in this line reaches a higher value in the 1st component than in the 4th one, the large depth of the 4th component provides it with the main contribution to the intensity of this line. The behavior of this emissivity within the 4th component, obtained from the c08.00 and c23.01 codes, is quite similar, except for the relatively thin outer part near the ionization front (see above). The differences in emissivities from these codes in the 2nd component are mainly caused by various artificial preservation issues in the calculation process for very small numbers: in the case of c08.00, this corresponds to a level of 10^{-36}, while in c23.01 it corresponds to 10^{-46} (similar numerical artifacts also arise in the inner part of the 1st component and the outer part of the 4th component). The differences in the 3rd component are quite small, reaching only $0.08-0.18$ dex. It should be noted that the c08.00 results show a higher emissivity of this line in the 3rd component compared to c23.01. This is the opposite of the situation in the 1st and 2nd components, where temperature is defined by hydrodynamical processes (shock propagation), while in the 3rd and 4th components, this value is defined by photoionization due to ionizing radiation transfer.

As a result, the emission line spectra calculated using the c08.00 and c23.01 releases of the CLOUDY code were obtained. The most important diagnostic emission line ratios are given in Table 1. It can be seen that the deviations of the new results from the old ones do not exceed 6.3%, while the corresponding observational error bars are often larger than 10%. Therefore, it can be concluded that c08.00 can be used as a 'path-finder' before calculating a large MPhM grid in parametric space. Furthermore, the results obtained using the c08.00 code, under the assumptions made in this work (spherical symmetry, etc.), are sufficiently reliable to draw physically sound conclusions.

4. Conclusions

The aim of the present work was to investigate the reliability of results obtained previously using MPhM of NebEns based on the old c08.00 version of the CLOUDY code, as well as to estimate whether it can be used in so-called 'path-finder' modeling before estimating the parametric space characterizing the

ionization structure and chemical abundances of HII regions surrounding active star-forming regions. This possibility is important because c08.00 is faster than c23.01 during MPhM of these objects.

To achieve this aim, a new wrapper for MPhM of NebEns based on the CLOUDY c23.01 code was developed, and the evolutionary chain of models was calculated using both MPhM wrappers based on the new c23.01 and the old c08.00 releases of the CLOUDY code.

By comparing the Lyα-spectra transformation in both results, it was concluded that c08.00 contains two 'phantom' emission lines in the photon energy range between 5 Ry and 6 Ry, which are absent in the spectrum of c23.01. It must be noted that the new version of CLOUDY has a much higher photon energy resolution grid and is free from bugs in the code, including the one described in the Introduction. Therefore, its spectrum is more accurate than that of c08.00.

The detailed comparison of the ionization structures obtained using these codes allowed us to conclude that the radial dependences of electron temperature and density, as well as the emissivities of important diagnostic recombination and emission lines, retain their character in the new models. Nevertheless, it was demonstrated that the role of the first component of MPhM (closest to star-forming regions) is higher than it was predicted by the old version of the code. It was also noted that technical assumptions in the codes, aimed at preserving stability during operations with very small numbers, impact the results for the second component much more strongly in the old version of the code. Additionally, it was shown that the thicknesses of both the third and fourth components calculated using c23.01 are larger than those calculated by c08.00.

To estimate the integral effect of the described differences on the overall results, we compared the modeling emission line spectra obtained with the new and old versions of the CLOUDY code. These spectra contain the relative intensities important for nebular diagnostics. It can be seen from Table 1 that the deviations of these results do not exceed 6.3%. In most cases, such deviations are within the observed range for the given emission lines. Therefore, it can be concluded that MPhM results obtained using the c08.00 code under the assumptions accepted in this work (spherical symmetry, etc.) are sufficiently reliable to draw physically sound conclusions. Thus, it can be used as a fast "path-finder" before calculating a large MPhM grid in the NebEn parametric space.

We plan to use both wrappers for MPhMs, based on c08.00 (as a path-finder) and c23.01 (for large parametric grid calculations) releases of the CLOUDY code, for investigating the stellar SED transformations within the first dwarf galaxies in the Universe embedded in dark matter halos.

[1] Osterbrock D. E., Ferland G. J. Astrophysics of Gaseous Nebulae and Active Galactic Nuclei. Second Edition. Saulito, California, University Science Book (2005).

[2] Ferland G. J. Hazy, a Brief Introduction to Cloudy. University of Kentucky, Physics Department Internal Report (2008).

[3] Koshmak I. O., Melekh B. Ya. Modelling of emission of H II region with bubble-like structure inside. Kinematics and Physics of Celestial Bodies. **29** (6), 257–268 (2013).

[4] Koshmak I. O., Melekh B. Ya. Multicomponent simulation of emission of low-metalicity H II regions. Kinematics and Physics of Celestial Bodies. **30** (2), 70–84 (2014).

[5] Koshmak I. O., Melekh B. Ya. Modelling of H II region radiation surrounding the starburst knot taking into account the structures evolution formed by superwind. Kinematics and Physics of Celestial Bodies. **33** (2), 39–54 (2017).

[6] Melekh B., Recchi S., Hensler G., Buhajenko O. Photoionization analysis of chemodynamical dwarf galaxies simulations. Monthly Notices of the Royal Astronomical Society. **450** (1), 111–127 (2015).

[7] Chevalier R. A., Clegg A. W. Wind from a starburst galaxy nucleus. Letters to Nature. **317**, 44–45 (1985).

[8] Weaver R., McCray R., Castor J., Shapiro P., Moore R. Interstellar bubbles. II. Structure and evolution. The Astrophysical Journal. **218**, 377–395 (1977).

[9] Atek H., Labbé I., Furtak L. J., et al. Most of the photons that reionized the Universe came from dwarf galaxies. Nature. **626**, 975–978 (2024).

[10] Gunasekera Ch. M., van Hoof P. A. M., Chatzikos M., Ferland G. J. The 23.01 Release of Cloudy. Research Notes of the AAS. **7** (11), 246 (2023).

[11] Kozel R. V., Melekh B. Ya. Transformation of energy distribution of ionizing radiation during penetrating very thin and dense envelope of nebular plasma. Visnyk of the Lviv University. Series Physics. **44**, 136–144 (2009), (in Ukrainian).

[12] Melekh B. Ya., Koshmak I. O., Kozel R. V. The influence of stellar wind bubbles on the radiation ionizing field in the nebular objects. Journal of Physical Studies. **15** (3), 3901 (2011).

[13] Koshmak I. O., Melekh B. Ya. The primordial helium abundance determination using multicomponent photoionization modelling of low-metalicity HII regions. Advances in Astronomy and Space Physics. **8** (1–2), 16–23 (2018).

[14] Tarter C. B. Radiative Transfer in a Gas Excited by X-Rays. Ph.D. Thesis, Cornell University. **28–10**, 3983 (1967).

[15] Leitherer C., Schaerer D., Goaldader J. D., et al. Starburst 99: Synthesis Models for Galaxies with Active Star Formation. Astrophysical Journal Supplement series. **123**, 3 (1999).

[16] Schaerer D., de Koter A., Schmutz W., Maeder A. Combined stellar structure and atmosphere models for massive stars. I. Interior evolution and wind properties on the main sequence. Astronomy and Astrophysics. **310**, 837–848 (1996).

[17] Schaerer D., de Koter A., Schmutz W., Maeder A. Combined stellar structure and atmosphere models for massive stars. II. Spectral evolution on the main sequence. Astronomy and Astrophysics. **312**, 475–495 (1996).

[18] Pauldrach A. W. A., Hoffmann T. L., Lennon M. Radiation-driven winds of hot luminous stars. XIII. A description of NLTE line blocking and blanketing towards realistic models for expanding atmospheres. Astronomy and Astrophysics. **375** (1), 161–195 (2001).

[19] Izotov Yu. I., Thuan T. X., Lipovetsky V. A. The primordial helium abundance from a new sample of metal deficient blue compact galaxies. The Astrophysical Journal. **435**, 647–667 (1994).

[20] Thuan T. X., Izotov Yu. I. High-ionization emission in metal-deficient blue compact dwarf galaxies. The Astrophysical Journal. **161**, 240–270 (2005).

[21] Pequignot D. Workshop on model nebulae. Publication de l'Observatoire de Meudon, Paris, ed. D. Pequignot (1986).

[22] Ferland G., Binette L., Contini M., et al. The Analysis of Emission Lines. Space Telescope Science institute Symposium Series, R. Williams & M. Livio, editors; Cambridge, Cambridge University Press (1995).

[23] Mathis J. S., Rumpl W., Nordsieck K. H. The size distribution of interstellar grains. The Astrophysical Journal. **217**, 425–433 (1977).

[24] Koshmak I. O., Melekh B. Ya. The role of dust in modelling the HII region emission with bubble-like structure inside. Journal of Physical Studies. **17** (4), 4901 (2013).

[25] Castor J., McCray R., Weaver R. Interstellar bubbles. The Astrophysical Journal. **200**, L107–L110 (1975).

[26] Melekh B., Buhajenko O., Koshmak I. Photoionization analysis of chemodynamical dwarf galaxies simulations. II. Detailed calculation of diffuse ionizing radiation. Monthly Notices of the Royal Astronomical Society. **532** (1), 524–537 (2024).

Мультикомпонентне фотоіонізаційне моделювання на основі програми Cloudy версій c23.01 та c08.00

Мелех Б. Я., Кошмак І. О.

Львівський національний університет імені Івана Франка, вул. Університетська, 1, 79000, Львів, Україна

Представлено нову версію програми для мультикомпонентного фотоіонізаційного моделювання світіння (МФМС) небулярного середовища (НС), що оточує область активного зореутворення, засновану на новій версії c23.01 коду Ґ. Ферланда CLOUDY. Наш підхід МФМС НС враховує внутрішню структуру зони HII та її еволюцію, спричинену розширенням супервітру. Розраховано еволюційну сітку МФМС НС, з використанням як нової, так і старої (заснованої на коді CLOUDY c08.00) версій програми. Зроблено порівняльний аналіз іонізаційної структури, емісійностей важливих для діагностики емісійних ліній, а також модельних спектрів, отриманих під час таких розрахунків, з метою оцінки впливу помилки у старій версії програми, пов'язаної з формуванням лінії Lyα, на результат МФМС НС. У результаті зроблено висновки щодо надійності результатів МФМС НС, отриманих за допомогою старої версії програми.

Ключові слова: *небулярне середовище; область зореутворення; фотоіонізаційне моделювання; моделі супервітру.*